International Journal on Magnetic Particle Imaging
Vol 12, No 1, Article ID 2607001, 7 Pages

Infinite Science Publishing

Research Article

Magnetic particle spectroscopy for breast cancer detection using AS1411-Nucleolin targeting

Hafiz Ashfaq Ahmad[a] · Ali Dinari[b] · Seungjun Oh[a] · Masoud Rezaie[c] · Jungwon Yoon[a,*]

[a]Department of AI Convergence, Gwangju Institute of Science and Technology, Gwangju, South Korea
[b]Department of Medical Physics, Jagiellonian University, ul. S. Lojasiewicza 11, 30-348, Krakow, Poland
[c]Department of Chemistry, Jagiellonian University, ul. S. Lojasiewicza 11, 30-348, Krakow, Poland
*Corresponding author, email: jyoon@gist.ac.kr

Received 03 November 2025; Accepted 07 May 2026; Published online 27 July 2026

Abstract

Magnetic particle spectroscopy (MPS) offers a rapid, wash-free means to transduce biomolecular binding into quantitative signals through Brownian-mobility changes of magnetic nanoparticles (MNPs). This study presents an MPS bioassay for breast cancer detection using aptamer AS1411-functionalized, carboxylated iron-oxide nanoparticles that recognize nucleolin (a breast cancer marker). A dual-stage scheme is implemented: (i) probe formation using EDC/NHS coupling of amine-terminated AS1411; (ii) secondary recognition of nucleolin. Conjugation was verified by DLS (hydrodynamic size increase; PDI < 0.30), and iron content was equalized by ICP-MS to ensure that MPS signals reflect conjugation. Primary conjugation produced monotonic attenuation of odd harmonics with aptamer density, with the third harmonic showing the most significant change (-67.0% vs plain MNPs). Secondary recognition yielded additional concentration-dependent declines (-59.9% at 100 nM relative to the MNP-aptamer baseline). MPS thus offers a robust, label-free readout with real-time acquisition and practical thresholds for breast-cancer markers, supporting clinical validation and portable point-of-care use.

I. Introduction

Breast cancer remains a major global health burden, where earlier and minimally invasive detection could meaningfully improve outcomes [1, 2]. Current clinical practice relies on imaging: mammography, ultrasound, and MRI, but each modality has well-recognized limitations: mammographic sensitivity declines in dense breasts [3], ultrasound performance varies with operator skill [4], and MRI entails higher cost, limited access, and contrast-agent considerations [5]. Serum proteins (CA15-3, CEA, HER2-ECD) are useful for monitoring but are not recommended for screening owing to limited standalone sensitivity and specificity, and to their reliance on multi-step, wash-based workflows [6]. Liquid-biopsy assays (ctDNA/CTCs/EVs) provide molecular resolution but face pre-analytical variability, technical complexity, and longer turnaround times, particularly in early disease with low analyte fractions [7, 8]. Beyond imaging, blood-borne biomarkers and circulating tumor-derived signals offer windows into disease presence and dynamics [9, 10]. MNP-based readouts are attractive in this context because they interrogate tracer physics directly with minimal tissue background [11, 12].

MPS is a zero-dimensional magnetic particle imaging (MPI) that quantifies the nonlinear magnetization of

superparamagnetic nanoparticles under an AC field [13, 14]. The harmonic response reflects two relaxation mechanisms: Néel (moment flipping) and Brownian (whole-particle rotation) [15]. For single-core iron-oxide particles with core sizes greater than 20 nm, Brownian relaxation dominates and is exquisitely sensitive to hydrodynamic size and microviscosity [16, 17]. MPS has been applied to protein, nucleic acid, and viral antigen sensing by exploiting size and viscosity-dependent changes in Brownian mobility that manifest as odd-harmonic attenuation or phase shifts; representative demonstrations and reviews detail real-time operation in buffer and serum surrogates [18, 19]. By contrast, MPI for in vivo imaging provides tracer-only contrast for tumor and lymphatic applications, with clinical relevance in breast imaging, including sentinel lymph node (SLN) mapping using iron-oxide tracers and related magnetic localization tools [11]. However, breast-focused biomarker assays using MPS remain sparse: studies explicitly targeting breast-associated analytes are limited, with few reports providing clinically interpretable figures of merit [13]. These gaps motivate a rigorously controlled, breast-relevant MPS assay that isolates relaxation physics and yields quantitative readouts, setting the stage for the work presented here.

This study presents an MPS system for breast cancer detection using AS1411, a G-rich DNA aptamer with high affinity to nucleolin, a protein frequently overexpressed on breast cancer cells [20]. A dual-stage workflow is implemented: first, covalent coupling of amine-terminated AS1411 to carboxylated MNPs produces stable, monodisperse recognition probes; second, post-conjugation blocking followed by target recognition to preserve ligand presentation and maximize Brownian-mobility hindrance upon specific binding [18]. Conjugation is verified by DLS, while the iron content of plain and conjugated MNPs is quantified by ICP-MS to normalize all assays to equal Fe mass before MPS measurement, ensuring that observed signal changes arise from relaxation dynamics rather than magnetic-mass variability [19]. Target-induced size increases then yield robust, analyte-dependent harmonic shifts in real-time, establishing a technically rigorous foundation for MPS as a sensitive, specific platform for breast-cancer screening and monitoring [13, 21].

II. Materials and methods

Carboxyl iron oxide nanoparticles (SHP25-02, Lot No: 040721) were purchased from Ocean Nano Tech Inc. (USA). MES (2-(N-Morpholino) ethanesulfonic acid hydrate, CAS No: 4432-31-9), EDC (1-Ethyl-3-(3-dimethylaminopropyl) carbodiimide), and NHS (N-Hydroxysuccinimide), were purchased from Sigma-Aldrich (South Korea). Phosphate-buffered saline (PBS) (Catalog No. 10010031) and deionized (DI) water were purchased from Thermo Fisher Scientific. AS1411 aptamer (A 26-base guanine-rich oligodeoxynucleotide aptamer) with a pre-modified terminal primary amine (-NH_2) was purchased from Bio-Synthesis Inc. (USA). Nucleolin protein was purchased from Sino Biological Inc. (China).

The MPS device was designed and fabricated in the Intelligent Medical Robotics Lab at GIST (South Korea). It has optimized excitation coils and highly sensitive receiver coils to detect the emitted signals from MNPs. Samples were excited with a 2 mT at 7.74 kHz frequency applied through a signal generator, a power amplifier (AE Techron 7724), and a bandpass excitation filter to ensure single-tone drive. The receive chain consisted of matched pickup coils and a DSP lock-in amplifier (SR865A, 4 MHz) for demodulating the third and fifth harmonics. Signals were digitized through NI PXIe-7867 and PCIe-6363 modules (National Instruments, Austin, TX). The system could detect MNPs at concentrations as low as 1 ng in 20 seconds with integrated frames. This demonstrates the system's potential for sensitive measurements in biological applications [19].

Conjugation of biomolecules to carboxyl-functionalized iron oxide nanoparticles (COOH-MNPs) was performed using the EDC/NHS coupling method [22]. Briefly, 200 µl of COOH-MNPs (SHP-25, 5 mg/mL; manufacturer's stock concentration) were activated in 100 mM MES buffer (pH 6.5) containing 10 mM EDC and 5 mM NHS and incubated for 10 minutes. Subsequently, the activated nanoparticles reacted with amine-terminated AS1411 to yield covalent amide linkages. The AS1411 aptamer was pre-modified with a terminal amine group to facilitate covalent attachment. Following aptamer conjugation, particles were washed multiple times with PBS to remove unreacted species. Washing was performed by magnetic separation using a permanent magnet, followed by removal of the supernatant and resuspension of the nanoparticle pellet in fresh buffer. No additional chemical blocking agent was applied; instead, surface stabilization was achieved through washing and buffer exchange before MPS measurements.

After the conjugation, dynamic light scattering (DLS; Zetasizer Nano ZSP, Malvern Panalytical) analysis was performed. DLS was conducted at room temperature on dispersions (50–100 µg/mL total solids). For comparative analyses, the nanoparticle content per measurement was kept constant, while varying the aptamer density (100 nM, 500 nM, 1 µM). Zeta potential measurements were performed using the same instrument immediately after conjugation and purification. Samples were magnetically washed three times with PBS and re-suspended in DI water before measurement to minimize buffer-related screening effects. Under these aqueous conditions, any NHS-active esters generated during EDC/NHS activa-

10.18416/ijmpi.2026.2607001

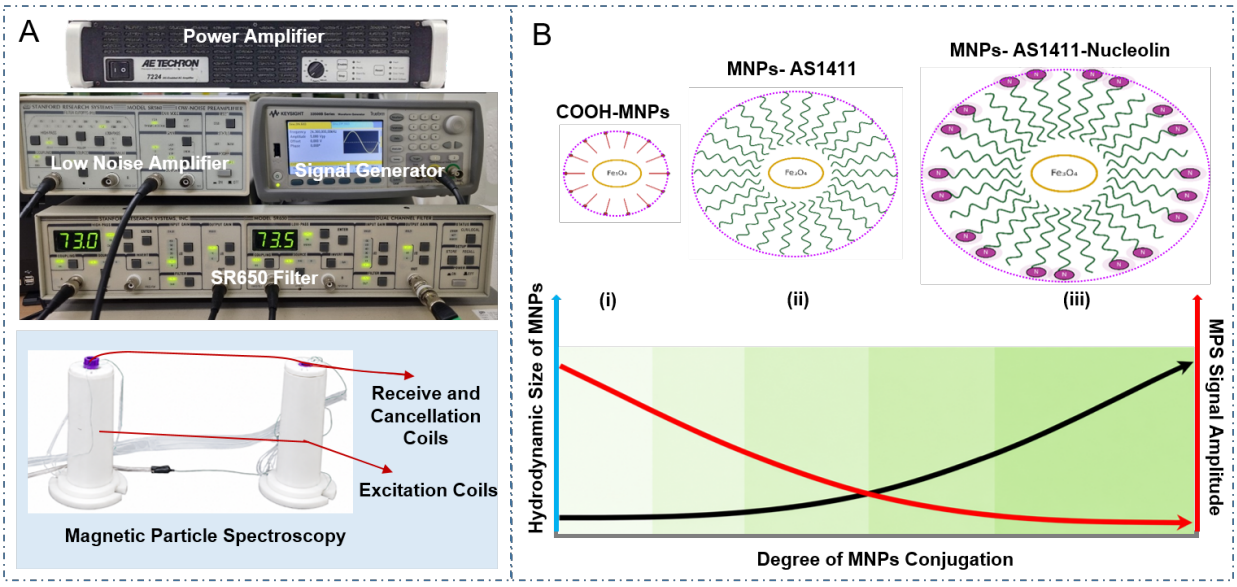

Figure 1: Overview of the developed MPS system. (A) shows the physical hardware of the MPS system, highlighting the signal generator, power amplifier, lock-in amplifier, and other components. (B) Assay principle: COOH-MNPs → AS1411-MNPs → AS1411–nucleolin complexes. Target binding increases hydrodynamic size/cluster formation, which suppresses Brownian rotation and yields a monotonic decrease in MPS harmonic amplitude.

Table 1: Sample's details for the detection of targeted nucleolin

Sample Name	Aptamer (nM)	Nucleolin (nM)	Fe mass (µg)
MNPs-Aptamer	100	0	20
MNPs-Aptamer + Nucleolin	100	25	20
MNPs-Aptamer + Nucleolin	100	50	20
MNPs-Aptamer + Nucleolin	100	75	20
MNPs-Aptamer + Nucleolin	100	100	20
MNPs-Aptamer + Nucleolin	100	150	20

Table 2: Hydrodynamic Size and Zeta Potential Values of Unmodified and Conjugated MNPs.

Parameters	Pure MNP	Aptamer		
Biomolecules concentration		100 nM	500 nM	1 uM
Size (nm)	51	52.3	59.14	69.55
PDI	0.122	0.142	0.194	0.181
Zeta potential (mV)	-22.9	-13.9	-15.26	-16.36

tion are expected to hydrolyze rapidly during washing and handling. Therefore, the measured zeta potential reflects the net surface charge after conjugation rather than transient activated intermediates.

To ensure that MPS readouts reflected relaxation dynamics rather than magnetic-mass variation, iron content in plain and conjugated formulations was quantified by ICP-MS (Agilent 7900, Japan) after microwave digestion (Multiwave 7000, Anton Paar) and used to normalize all samples to an identical Fe mass before measurement [19]. Conjugates were magnetically separated, washed, and re-suspended in 200 µL PBS; 10 µL aliquots were digested with 1,000 µL HNO_3, diluted to volume, and analyzed against external Fe standards and blanks.

MPS assays were conducted in two tiers. Sensitivity to primary conjugation was profiled by preparing MNP-aptamer probes at concentrations of 12.5, 25, 50, 100, and 500 nM aptamer and recording the third and fifth harmonic responses. Secondary binding was then evaluated using probes made with a 100 nM aptamer and adding nucleolin at concentrations of 25, 50, 75, 100, and 150 nM to quantify target-induced harmonic modulation under equal-iron loading conditions. All MPS measurements were performed using ten independent samples per condition (n = 10). Statistical analysis was conducted using analysis of variance (ANOVA), followed by pairwise t-tests for post hoc comparisons where applicable. Statistical significance was defined as $^{*}p < 0.05$, $^{**}p < 0.01$, and $^{***}p < 0.001$. Error bars in all figures represent the standard deviation across independent samples. The sample's details are shown in Table 1. A complete experimental setup is shown in Figure 1.

III. Results and discussion

Hydrodynamic and interfacial changes upon functionalization were quantified by DLS (Figure 2; Table 2). The mean hydrodynamic diameter increased from 51 nm for unmodified particles to 59 nm following aptamer conju-

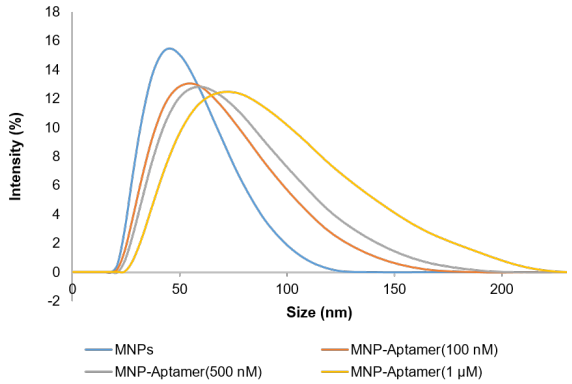

Figure 2: Hydrodynamic size distribution of MNPs after aptamer conjugation measured by DLS. In all cases, conjugation resulted in a concentration-dependent increase in hydrodynamic diameter, consistent with surface modification of the nanoparticles following biomolecule attachment.

gation, with a simultaneous shift in zeta potential consistent with surface chemistry alteration. Across aptamer-density series, all conjugates exhibited size increases compatible with successful surface coverage. Polydispersity indices (PDI) remained <0.30 for all conditions, indicating moderately monodisperse suspensions with minimal aggregation and acceptable colloidal stability for downstream magnetic measurements.

The increase in zeta potential magnitude from -22.9 mV (plain MNPs) to -13.9 mV at low aptamer coverage is consistent with partial charge screening and surface neutralization upon ligand grafting, while the modest decrease observed at higher aptamer concentrations likely reflects the increasing contribution of the negatively charged phosphate backbone of the DNA aptamer. Such non-monotonic trends have been reported previously for polyanionic biomolecules conjugated to carboxylated nanoparticle surfaces and reflect competing surface-chemistry effects rather than experimental artifacts.

The observed increase in hydrodynamic diameter following aptamer functionalization is consistent with surface modification of the nanoparticles, indicating the presence of biomolecules at the interface. However, it is noted that DLS alone does not verify covalent bond formation; rather, it provides supportive evidence of interfacial changes that must be interpreted alongside the applied EDC/NHS chemistry, zeta potential shifts, and the functional MPS response.

For DLS measurements, untreated COOH-MNPs (no EDC/NHS activation) were used as the reference sample, while all aptamer-conjugated samples were processed identically through EDC/NHS activation and washing prior to analysis.

To isolate relaxation-driven effects from variability in magnetic loading, iron content was quantified by ICP-MS

Table 3: Iron concentration (mg/mL) of Aptamer-conjugated MNP samples measured by ICP-MS. Results show the mean ± SD of three replicates and the percentage of Fe retained relative to the original MNPs.

Sample	Rep-1 Fe	Rep-2 Fe	Rep-3 Fe	Mean ± SD (mg/mL)	% Fe Retained
	(mg/ml)				
Plain MNPs	3.200	3.152	3.17	3.18 ± 0.034	100%
MNPs-Aptamer	1.010	1.006	1.008	1.01 ± 0.003	31.8%

and used to normalize all samples before MPS analysis. Plain MNPs measured 3.176 ± 0.034 mg Fe mL^{-1}, whereas MNP-aptamer formulations retained 31.7% of the original Fe following conjugation and washing (Table 3). For MPS assays targeting 20 µg Fe in 500 µL, volumes were calculated from the measured concentrations through (1), yielding 6.25 µL of plain MNPs and 19.71 µL of MNP-aptamer, with the remainder made up in DI water.

$$\text{Volume} = \frac{\text{Required Concentration (µg)}}{\text{ICP Determined Concentration (µg/µL)}} \quad (1)$$

This normalization ensured that subsequent signal changes reflected Brownian-mobility modulation rather than differences in magnetic mass.

ICP-MS analysis indicated that approximately 31.7% of the initial iron content was recovered after aptamer conjugation and purification. This reduction primarily reflects nanoparticle recovery during magnetic separation and washing, which can be substantial for ≈25 nm single-core MNPs, rather than limitations of the EDC/NHS coupling chemistry itself. Transient changes in surface charge and colloidal stability during activation and buffer exchange, together with handling losses during repeated washes, likely contribute to the reduced recoverable mass. Importantly, all MPS measurements were normalized to the recovered iron concentration to ensure that the reported signal changes arise from Brownian relaxation effects rather than from differences in magnetic mass.

Previous research has demonstrated that conjugation of biomolecules to MNP surfaces alters their hydrodynamic size and Brownian relaxation properties, thereby modulating the MPS response, particularly at higher-order harmonics [15, 18, 23]. Building on these findings, we systematically investigated the efficiency of our MPS system for aptamer-conjugated MNPs, to establish the detection and evaluate biomarker-specific interactions.

For primary conjugation, the third- and fifth-harmonic responses decreased monotonically with increasing ligand coverage (aptamer amount from 12.5 to 500 nM), with the third harmonic showing the most pronounced and statistically significant attenuation relative to plain MNPs (Figure 3) by performing ANOVA followed by pairwise t-tests for post-hoc comparisons. This

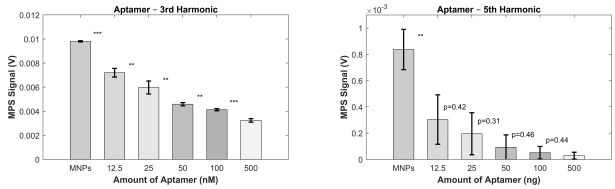

Figure 3: MPS signals (third and fifth harmonics) of MNPs conjugated with increasing concentrations of Aptamer. Significant reductions in third-harmonic signals confirm successful conjugation and an increase in hydrodynamic size, with p-values indicating statistical significance. The fifth harmonic shows weaker sensitivity, but the trend is the same.

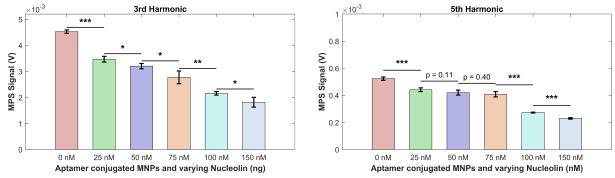

Figure 4: MPS signal response to secondary bioconjugation in the presence of first. Third and fifth harmonic analysis of MNPs-Aptamer samples following nucleolin conjugation. Signal reduction reflects successful dual-stage bioconjugation and reduced Brownian relaxation, with statistical significance indicated (*p < 0.05, **p < 0.01, ***p < 0.001).

trend indicates progressive hindrance of Brownian rotation as hydrodynamic size and interfacial drag increase upon ligand grafting. Significance annotations (*p < 0.05; **p < 0.01; ***p < 0.001) confirmed that these changes were resolvable within short integration windows, aligning with prior MPS biosensing reports that emphasize odd-harmonic metrics [23]. Collectively, these observations reinforce MPS as a promising transduction modality for label-free biosensing and diagnostics.

Secondary recognition was then assessed using aptamer-functionalized probes, with the primary aptamer loading fixed at 100 nM and the breast-cancer biomarker nucleolin varied at concentrations given in Table 1. The resulting bar plots (Figure 4) show concentration-dependent decreases in both third- and fifth-harmonic amplitudes, confirming specific secondary attachment. The signal drop reflects additional growth of the hydrodynamic envelope upon target binding, along with the accompanying suppression of Brownian relaxation. Notably, the third harmonic again provided the greatest dynamic range and statistical significance ($p < 0.05$ to $p < 0.001$), indicating sensitivity to early-stage molecular interactions on the nanoparticle surface. These results demonstrate that aptamer-conjugated MNPs effectively recognize and bind nucleolin, highlighting the applicability of MPS for breast cancer biomarker detection.

To verify that the observed harmonic attenuation results from specific AS1411–nucleolin recognition rather

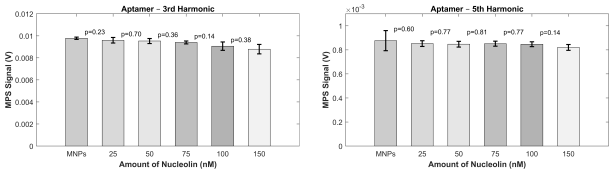

Figure 5: Third- and fifth-harmonic MPS responses of unconjugated COOH-MNPs upon incubation with nucleolin at varying concentrations (25–150 nM) under equal iron loading (20 µg Fe). No systematic or concentration-dependent signal attenuation is observed, indicating negligible non-specific interaction between nucleolin and COOH-MNPs in the absence of AS1411 aptamer.

than nonspecific protein adsorption, a control experiment was performed using unconjugated COOH-MNPs incubated with nucleolin at identical concentrations and iron loadings. As shown in Figure 5, plain MNPs exhibited no monotonic or statistically significant change in either the third- or fifth-harmonic amplitudes across the tested nucleolin range. This confirms that nucleolin alone does not measurably alter Brownian relaxation of COOH-MNPs and that the signal changes reported in Figure 4 originate from aptamer-mediated specific binding.

To quantitatively evaluate changes in binding-induced relaxation, the harmonic amplitudes were normalized to appropriate controls. The averaged attenuation values of the third harmonic signal are decreased by 67.0% for MNP–aptamer probes, indicating a substantial damping of Brownian mobility after ligand grafting. For secondary binding at 100 nM nucleolin, third-Harmonic amplitudes were reduced by 59.9% versus the aptamer-only baseline, establishing concentration-dependent recognition on an equal-iron basis. These behaviors align with established MPS mobility-analysis frameworks that use absolute amplitudes or harmonic-ratio metrics to parameterize binding-induced relaxation shifts [23].

Taken together, the data establish MPS as a dual-purpose readout: (i) indicating probe formation (primary conjugation) and (ii) sensitively transducing specific target engagement (secondary interaction) under rigorously iron-normalized conditions. Nucleolin is a breast-cancer–associated marker: a multifunctional phosphoprotein abundant in the nucleolus and aberrantly displayed on the cell surface in many tumors, including breast cancer, where it supports proliferation, survival, and metastatic programs [24]. Its elevated cell-surface presentation provides an accessible molecular handle for affinity ligands such as AS1411, a G-rich DNA aptamer with high binding specificity and favorable low immunogenicity [20, 25]. Binding of AS1411 to surface nucleolin increases the nanoparticle's hydrodynamic diameter and viscous drag; MPS converts this mobility change into a robust attenuation of the third harmonic within minutes, yielding a wash-free, label-free signal [18]. While

the present study establishes a rigorous proof of concept for aptamer-mediated nucleolin detection using MPS under controlled buffer conditions, performance in complex biological matrices such as serum or plasma was not evaluated here. In such environments, factors such as nonspecific protein adsorption (protein corona formation), increased viscosity, and competing biomolecules may influence nanoparticle Brownian relaxation and assay sensitivity. Addressing these matrix effects through optimized surface passivation, blocking strategies, and calibration in biologically relevant media represents an important direction for future work toward clinical translation.

For breast cancer detection, this mechanism can be deployed in two complementary ways. First, it serves as a single-analyte screen for nucleolin-positive disease, enabling rapid monitoring of treatment response. Second, and more specifically, as part of a multiplex breast panel in which AS1411-MNPs are run alongside breast-oriented markers (CA15-3, CEA ± HER2-ECD) on separate channels, decision-level fusion then enhances disease specificity while preserving the nanomolar-level sensitivity demonstrated here [26, 27].

IV. Conclusions

This work demonstrates that MPS can transduce breast cancer–relevant molecular binding into a robust, quantitative signal in real time. Using AS1411-functionalized iron-oxide nanoparticles and strict iron-mass normalization, third-harmonic attenuation consistently reflected two stages: aptamer probe formation and specific nucleolin recognition, thereby linking Brownian mobility changes to the analytical readout. The platform is label-free, wash-free, and compatible with serum handling, supporting practical threshold and rapid workflows. Because nucleolin is frequently elevated in breast cancer, the assay provides a biologically grounded detection approach and can be configured for greater disease specificity by multiplexing with established breast markers (CA15-3, CEA, HER2-ECD). Overall, the results position MPS as a technically rigorous and robust modality under controlled buffer conditions, with clear potential for future clinical translation as a clinically promising modality for breast cancer detection and monitoring, motivating subsequent validation in patients and the development of portable instrumentation for point-of-care use.

Acknowledgments

This work was supported by the National Research Foundation of Korea (NRF) grant funded by the Korea government (MSIT) (No. RS-2025-00554248).

Author's statement

Conflict of interest: The Authors state that there is no conflict of interest.

References

[1] F. Bray, M. Laversanne, H. Sung, J. Ferlay, R. L. Siegel, I. Soerjomataram, and A. Jemal. Global cancer statistics 2022: GLOBOCAN estimates of incidence and mortality worldwide for 36 cancers in 185 countries. *CA: A Cancer Journal for Clinicians*, 74(3):229–263, 2024, doi:10.3322/caac.21834.

[2] O. Ginsburg, C.-H. Yip, A. Brooks, A. Cabanes, M. Caleffi, J. A. Dunstan Yataco, B. Gyawali, V. McCormack, M. McLaughlin De Anderson, R. Mehrotra, A. Mohar, R. Murillo, L. E. Pace, E. D. Paskett, A. Romanoff, A. F. Rositch, J. R. Scheel, M. Schneidman, K. Unger-Saldaña, V. Vanderpuye, T.-Y. Wu, S. Yuma, A. Dvaladze, C. Duggan, and B. O. Anderson. Breast cancer early detection: A phased approach to implementation. *Cancer*, 126(S10):2379–2393, 2020, doi:10.1002/cncr.32887.

[3] F. Bodewes, A. Van Asselt, M. Dorrius, M. Greuter, and G. De Bock. Mammographic breast density and the risk of breast cancer: A systematic review and meta-analysis. *The Breast*, 66:62–68, 2022, doi:10.1016/j.breast.2022.09.007.

[4] G. E. Chalouhi, V. Bernardi, A. Gueneuc, I. Houssin, J. J. Stirnemann, and Y. Ville. Evaluation of trainees' ability to perform obstetrical ultrasound using simulation: Challenges and opportunities. *American Journal of Obstetrics and Gynecology*, 214(4):525.e1–525.e8, 2016, doi:10.1016/j.ajog.2015.10.932.

[5] F. Pesapane, A. Sorce, O. Battaglia, C. Mallardi, L. Nicosia, L. Mariano, A. Rotili, V. Dominelli, S. Penco, F. Priolo, G. Carrafiello, and E. Cassano. Contrast Agents in Breast MRI: State of the Art and Future Perspectives. *Biomedicines*, 13(4):829, 2025, doi:10.3390/biomedicines13040829.

[6] V. B. Varzaru, A.-E. Eftenoiu, D. C. Vlad, C. S. Vlad, A. E. Moatar, R. Popescu, and I. M. Cobec. The Influence of Tumor-Specific Markers in Breast Cancer on Other Blood Parameters. *Life*, 14(4):458, 2024, doi:10.3390/life14040458.

[7] J. D. Merker, G. R. Oxnard, C. Compton, M. Diehn, P. Hurley, A. J. Lazar, N. Lindeman, C. M. Lockwood, A. J. Rai, R. L. Schilsky, A. M. Tsimberidou, P. Vasalos, B. L. Billman, T. K. Oliver, S. S. Bruinooge, D. F. Hayes, and N. C. Turner. Circulating Tumor DNA Analysis in Patients With Cancer: American Society of Clinical Oncology and College of American Pathologists Joint Review. *Archives of Pathology & Laboratory Medicine*, 142(10):1242–1253, 2018, doi:10.5858/arpa.2018-0901-SA.

[8] C. Théry, K. W. Witwer, E. Aikawa, *et al.* Minimal information for studies of extracellular vesicles 2018 (MISEV2018): A position statement of the International Society for Extracellular Vesicles and update of the MISEV2014 guidelines. *Journal of Extracellular Vesicles*, 7(1):1535750, 2018, doi:10.1080/20013078.2018.1535750.

[9] J. Xu, H. Gao, X. Guan, J. Meng, S. Ding, Q. Long, and W. Yi. Circulating tumor DNA: From discovery to clinical application in breast cancer. *Frontiers in Immunology*, 15:1355887, 2024, doi:10.3389/fimmu.2024.1355887.

[10] J. Qiu, D. Qian, Y. Jiang, L. Meng, and L. Huang. Circulating tumor biomarkers in early-stage breast cancer: Characteristics, detection, and clinical developments. *Frontiers in Oncology*, 13:1288077, 2023, doi:10.3389/fonc.2023.1288077.

[11] X. Y. Zhou, Z. W. Tay, P. Chandrasekharan, E. Y. Yu, D. W. Hensley, R. Orendorff, K. E. Jeffris, D. Mai, B. Zheng, P. W. Goodwill, and S. M. Conolly. Magnetic particle imaging for radiation-free, sensitive and high-contrast vascular imaging and cell tracking. *Current Opinion in Chemical Biology*, 45:131–138, 2018, doi:10.1016/j.cbpa.2018.04.014.

[12] J.-H. Kim, J.-H. Kim, H. A. Ahmad, H. Kim, R. Nagareddy, K.-H. Choi, J. Yoon, and Y.-Y. Jeong. Effects of atorvastatin-loaded PEGylated liposomes delivered by magnetic stimulation for stroke treatment. *Brain Stimulation*, 18(5):1620–1631, 2025, doi:10.1016/j.brs.2025.08.024.

[13] P. Yari, B. Rezaei, C. Dey, V. K. Chugh, N. V. R. K. Veerla, J.-P. Wang, and K. Wu. Magnetic Particle Spectroscopy for Point-of-Care: A Review on Recent Advances. *Sensors*, 23(9):4411, 2023, doi:10.3390/s23094411.

[14] H. A. Ahmad, H. Kim, J.-H. Kim, K.-H. Choi, and J. Yoon. Advancing brain drug delivery: Focused magnetic hyperthermia and magnetic particle imaging for real-time BBB modulation. *International Journal on Magnetic Particle Imaging IJMPI*, 11(1), 2025, doi:10.18416/IJMPI.2025.2508004.

[15] J. Zhong, K.-J. Janssen, S. Draack, T. Viereck, M. Schilling, and F. Ludwig. Dependence of biomolecule detection on magnetic nanoparticle concentration. *Journal of Magnetism and Magnetic Materials*, 517:167408, 2021, doi:10.1016/j.jmmm.2020.167408.

[16] L. Maldonado-Camargo, M. Unni, and C. Rinaldi, Magnetic Characterization of Iron Oxide Nanoparticles for Biomedical Applications, in *Biomedical Nanotechnology*, S. H. Petrosko and E. S. Day, Eds., 1570, New York, NY: Springer New York, 2017, 47–71, ISBN: 978-1-4939-6838-1 978-1-4939-6840-4. doi:10.1007/978-1-4939-6840-4_4.

[17] H. A. Ahmad and J. Yoon. Comparative Evaluation of Relaxation-Based Bio-Sensing Performance of Magnetic Nanoparticles Using Magnetic Particle Spectroscopy. *IEEE Transactions on NanoBioscience*, 25(2):191–202, 2026, doi:10.1109/TNB.2025.3640088.

[18] X. Zhang, D. B. Reeves, I. M. Perreard, W. C. Kett, K. E. Griswold, B. Gimi, and J. B. Weaver. Molecular sensing with magnetic nanoparticles using magnetic spectroscopy of nanoparticle Brownian motion. *Biosensors and Bioelectronics*, 50:441–446, 2013, doi:10.1016/j.bios.2013.06.049.

[19] A. Dinari, H. A. Ahmad, S. Oh, Y.-H. Kim, and J. Yoon. Advanced Detection of Pancreatic Cancer Circulating Tumor Cells Using Biomarkers and Magnetic Particle Spectroscopy. *Nanotheranostics*, 9(2):171–185, 2025, doi:10.7150/ntno.110074.

[20] J. Prakash and K. Rajamanickam. Aptamers and Their Significant Role in Cancer Therapy and Diagnosis. *Biomedicines*, 3(3):248–269, 2015, doi:10.3390/biomedicines3030248.

[21] A. Dinari, H. Ashfaq Ahmad, M. P. Bùi, S. Oh, Y.-H. Kim, D.-H. Kim, and J. Yoon. Targeted Cellular Tracking of Pancreatic Cancer Cells via Magnetic Particle Spectroscopy (MPS). *Bio-Algorithms and Med-Systems*, 20(Special Issue):63–70, 2024, doi:10.5604/01.3001.0054.9363.

[22] G. T. Hermanson, Bioconjugate Techniques, Third edition. London ; Waltham, MA: Elsevier/AP, 2013, ISBN: 978-0-12-382239-0.

[23] S. Ota and Y. Takemura. Characterization of Néel and Brownian Relaxations Isolated from Complex Dynamics Influenced by Dipole Interactions in Magnetic Nanoparticles. *The Journal of Physical Chemistry C*, 123(47):28859–28866, 2019, doi:10.1021/acs.jpcc.9b06790.

[24] S. Thongchot, K. Aksonnam, P. Thuwajit, P.-T. Yenchitsomanus, and C. Thuwajit. Nucleolin-based targeting strategies in cancer treatment: Focus on cancer immunotherapy (Review). *International Journal of Molecular Medicine*, 52(3):81, 2023, doi:10.3892/ijmm.2023.5284.

[25] A. Van Den Avont and N. Sharma-Walia. Anti-nucleolin aptamer AS1411: An advancing therapeutic. *Frontiers in Molecular Biosciences*, 10:1217769, 2023, doi:10.3389/fmolb.2023.1217769.

[26] Y. Fu and H. Li. Assessing Clinical Significance of Serum CA15-3 and Carcinoembryonic Antigen (CEA) Levels in Breast Cancer Patients: A Meta-Analysis. *Medical Science Monitor*, 22:3154–3162, 2016, doi:10.12659/MSM.896563.

[27] N. Reix, C. Malina, M.-P. Chenard, J.-P. Bellocq, S. Delpous, S. Molière, A. Sevrin, K. Neuberger, C. Tomasetto, and C. Mathelin. A prospective study to assess the clinical utility of serum HER2 extracellular domain in breast cancer with HER2 overexpression. *Breast Cancer Research and Treatment*, 160(2):249–259, 2016, doi:10.1007/s10549-016-4000-z.

